Journal of Aerosol Science 94 (2016) 9–21

Contents lists available at ScienceDirect

Journal of Aerosol Science

journal homepage: www.elsevier.com/locate/jaerosci

Charge distribution of welding fume particles after charging by corona ionizer

V.I. Vishnyakov*, S.A. Kiro, M.V. Oprya, A.A. Ennan

Physical-Chemical Institute for Environmental and Human Protection, National Academy of Sciences of Ukraine, 3 Preobrazhenskaya, Odessa 65082, Ukraine

ARTICLE INFO

Article history:
Received 9 December 2014
Received in revised form
9 December 2015
Accepted 11 December 2015
Available online 18 December 2015

Keywords:
Unipolar charging
Differential mobility analyzer
Welding fume plasma
Size distribution
Charge distribution

ABSTRACT

An experimental technique, including the differential mobility analyzer and laser aerosol spectrometer, is proposed for determining the aerosol particles charge distribution, charged by the corona discharge. Experimental data processing procedure for determining the polydisperse welding fume particles charge distribution is proposed. Unipolar particle charging process in the environment saturated by ions is studied. Proposed theoretical model of unipolar charging in approximation of the dust–ion plasma demonstrates good correlation with experimental data. The two-dimensional size and charge distributions of welding fume particles are demonstrated.

1. Introduction

The particles' charging control is of great importance for aerosol science and technology. Indoor air cleaners, industrial electrostatic precipitators, and smoke detectors are instances of practical apparatuses and instruments, which ultimately rely upon the capability of airborne particles to acquire a net electric charge (Alonso, Santos, Hontañón, & Ramiro, 2009). Particulates in the exhausts from industrial processes are either uncharged or weakly charged both positively and/or negatively, depending on their previous history. Therefore, aerosol particles need charging by unipolar ions for their effective electrostatic precipitation. Unipolar charging has advantage over bipolar charging (by radioactive sources or UV-radiation) as it enables the attainment of a higher charging efficiency (Kruis & Fissan, 2001). Corona discharge is among the most common technique to produce high number density of unipolar ions and it is used in many industrial applications such as electrostatic coating and precipitation (Sparks, 1988); in determining aerosol size distribution by electrical mobility analysis (Biskos, Reavell, & Collings, 2005b; Tammet, Mirme, & Tamm, 2002).

The arc welding processes are accompanied by formation of toxic welding fumes, representing the danger for human health and environment. As a result, the harmful welding fume must be collected and treated before entering the worker's breathing zone. Welding fume inhaled particles range in the size from 0.002 to 5 μm as a result of different particle formation mechanisms (Vishnyakov, Kiro, Oprya, & Ennan, 2014). Particles fraction below 0.1 μm in mass distribution corresponds to a very small, nearly negligible part of generated mass. The primary particles agglomerates with different spatial structures and sizes over 0.1 μm and coarse fume particles mostly prevail in the welder's breathing zone (Berner & Berner, 1982; Sowards, Lippold, Dickinson, & Ramirez, 2008a).

* Corresponding author. Tel.: +380 487237528; fax: +380 487231116.
E-mail addresses: drvishnyakov@mail.ru, eksvar@ukr.net (V.I. Vishnyakov).

http://dx.doi.org/10.1016/j.jaerosci.2015.12.003
0021-8502/

Portable electrostatic precipitators are ideally suited for welding fume collection if the air is to be returned into the workspace. They require very little maintenance and do not need expenses for periodic cartridge filter replacement (Ravent, 2006). But the electrostatic precipitator collection efficiency reaches a minimum for particles in the 0.1–0.2 μm size range (Cheng, Yeh, & Kanapilly, 1981) and reflects the size-dependent combined field and diffusion charging behavior (Hinds, 1999) in transition regime ($0.1 < \mathrm{Kn} < 1$), to which the welding fume particles belong. For different welding and cutting processes, the median of welding fume particle size distribution is in the range 0.1–0.25 μm; the mass median aerodynamic diameter is in the range 0.2–0.45 μm (Pohlmann, Holzinger, & Spiegel-Ciobanu, 2013). The particle size distribution in the worker's breathing zone (at a distance of 40 cm from the welding arc) does not change during the process.

The particles' morphology influence their charging rate (Oh, Park, & Kim, 2004; Shin et al., 2010). Besides, for a polydisperse aerosol, the charge distribution of various-size particles will depend upon the size distribution peculiarities (Hoppel & Frick, 1986). The ability of welding fume particles to acquire a net charge in the corona discharge, their size and charge distributions determine the electrostatic parameters of their separation and precipitation, for which the high charges of particles are necessary. Therefore, the feasibility of measuring the particle charge distribution in the range of high charges has great practical interest. The particle charges measurement is usually based on a certain theoretical model of the particle charging. The Fuchs limiting-sphere theory (Fuchs, 1963) is the most commonly used for particle charging in the transition regime. However, this theory is inapplicable for systems with high ion number density, which is necessary for obtaining high particle charges. For example, inapplicability of the Fuchs theory for ion number density exceeding $10^7\ \mathrm{cm}^{-3}$ is demonstrated in the paper by Biskos, Reavell, and Collings (2005a). Therefore, the study of the welding fume particles charging by the corona discharge has great importance to achieve the portable electrostatic precipitators optimal design.

Especially important is a separation of particles by sizes during their collection, because the welding fume dust fine fractions is a valuable raw material, which is suitable for some industrial applications. For example, these fractions, which contain the transition metal oxides, can be used for the manufacturing of catalysts without any special treatment, in particular, for the ozone decomposition reaction (Rakitskaya, Ennan, Truba, Kiro, & Volkova, 2014).

In the present paper, the experimental equipment in which a long differential mobility analyzer (DMA) is supplemented by the laser aerosol spectrometer LAS-P (LAS-P, 2010) is used for measuring the welding fume particle charges in the size range 0.15–1.5 μm. The mobility-equivalent particle diameter, determined from DMA, in general case is not equal to optical diameter, determined with LAS-P. However, Emets, Kascheev, and Poluektov (1991) used such a tandem system already, and has demonstrated correctness of these diameters comparison in the range of 0.3–10 μm.

A theoretical model of unipolar particle charging in the environment saturated by ions is proposed and two-dimensional welding fume particle size and charge distributions are obtained. These results are intended, basically, for portable electrostatic precipitator designing, which can separate the particles by sizes in the process of their collection.

2. Corona discharge ionizer

The corona discharge ionizer (corona charger) used for particles' charging is shown in Fig. 1. The ionizer consists of coaxial inner multi-needle discharge electrode and grounded housing with an inner radius 53 mm (8). This configuration provides the annular aerosol flow with 300 Lpm flow rate. The discharge electrode has six steel disks (5) with 32 mm radius and 2 mm thickness; and each one contains fifteen stainless steel needles with the tip radius of 25 μm (6) radially mounted and connected to a high-voltage power supply. The needle tips are equally spaced on a 38 mm radius circle. The distances from the needle tips to the grounded housing are 15 mm.

Disks with needles are mounted between the special designed insulated holders (4) so the needles are in the ring channel with a width 8 mm and depth 6 mm into which the sheath air enters through the axial hole (7). The sheath air with a flow rate of 5 Lpm is used to prevent the aerosol particles from entering into the high-intensity corona region.

The distance between the disks with needles is 17 mm. The needles into each subsequent disc were pre-placed with a displacement 4° in respect to the needles of the previous disc, i.e. all aerosol particles pass through the identical ion number density corona regions. Such a design of the multi-needle discharge electrode provides the low threshold voltage (~3.2 kV) and a high power of corona discharge. The measured current of corona discharge is used for estimate the average ion number density.

The aerosol flow with rate $Q_I \cong 301$ Lpm enters into the corona ionizer through the axial channel (1), and into the charging region through the four tangential holes. The cross-section of charging region is $S_I = 38\ \mathrm{cm}^2$, and length is $L_I = 120$ mm. The particle charging time in the ionizer is $t_I \cong 80$ ms. The sheath air with a flow rate of 50 Lpm also enters into the charging region along the inner surface of housing through the inlet chamber (2) and the narrow annular channel (3), for the particles' loss minimization.

3. Experimental equipment

The experimental equipment schematic diagram used for the charge and size particle distribution measurement is shown in Fig. 2. It consists of four parts: a welding fume source; a corona charger; a differential mobility analyzer (DMA); and a laser aerosol spectrometer (LAS-P).

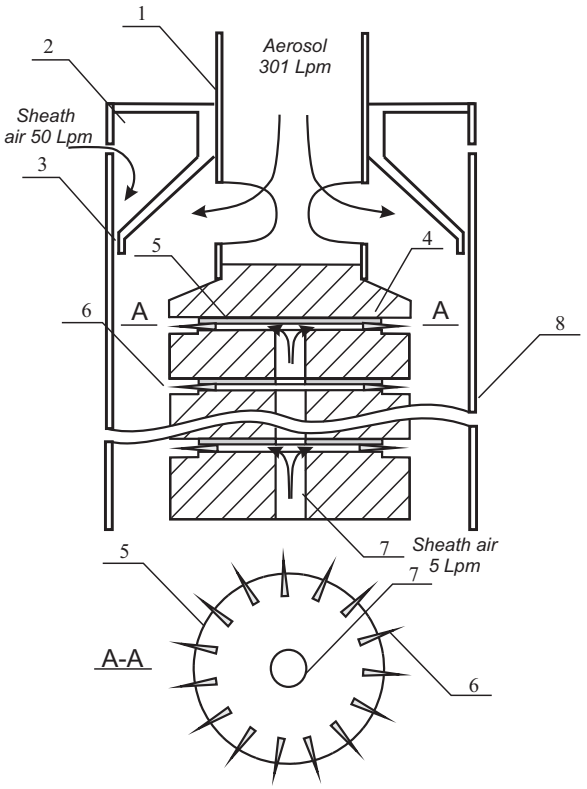

Fig. 1. Corona discharge ionizer.

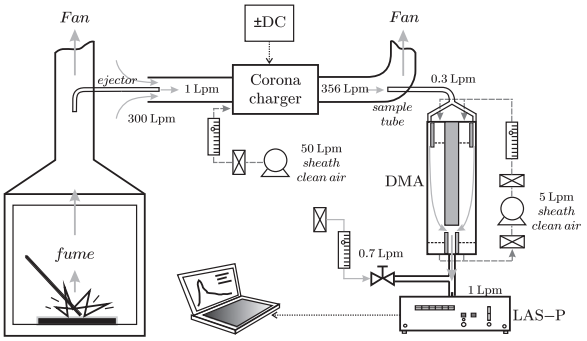

Fig. 2. Experimental equipment schematic diagram.

A welding fume source is a special chamber for shielded metal arc welding (SMAW) (Sowards, Lippold, Dickinson, & Ramirez, 2008b, 2010) under condition of reverse polarity direct current of 140 A and voltage of 33 V. The mild steel plates were used as a base material for single-pass welding. The SMAW commercial electrodes covered with carbonate–fluorite ($CaCO_3$–CaF_2) Paton UONI 13/55 (American Welding Society classification E6012) were used.

The welding fume plume was localized by extracting air at a distance of 40 cm from the welding arc with a flow of 75 Lps (Ennan, Kiro, Oprya, & Vishnyakov, 2013; Oprya et al., 2012) and the welding fume sample with flow rate of 1 Lpm is injected from the chimney center in a clean carrier air flow with 300 Lpm flow rate (Petryanov's filters with the collection efficiency of at least 99.97% for particles with a size of 0.15–0.2 μm were used for air cleaning). As a result of dilution the aerosol particle number density is decreased down to $\sim 5 \times 10^4$ cm^{-3}. The high degree of welding fume sample dilution (e.g. 430/1 and 1075/1) does not affect the particle size distribution (Ennan et al., 2013). This aerosol flow is passed through the corona charger, where unipolar charging by positive or negative ions takes place. The charged aerosol flow goes into the horizontal pipe with a diameter of 190 mm, in which the velocity profile in the center vicinity was measured by an anemometer (IS-2 in Russian classification). The air flow rate at the sampling point was 0.3 ± 0.1 m/s. The grounded tube for isokinetic sampling of aerosol with flow rate of 0.3 Lpm is used. Further, the charged particles are classified according to their electrical mobility by the DMA at different voltages. The DMA designed by Knutson and Whitby (1975) with recirculation of sheath

clean air (flow rate of 5 Lpm) is used. The direct voltage applied to the DMA varied with the step of 10 V for negative polarity and of 20 V for positive polarity.

The DMA extracts from the incoming aerosol charged particles with electrical mobility $Z = Z_0$, which depends on applied voltage U, the flow rate Q, and the geometric dimensions of DMA (Knutson & Whitby, 1975):

$$Z_0 = \frac{Q_s}{2\pi UL} \ln \frac{R_2}{R_1}, \tag{1}$$

where R_1 is the outer radius of DMA center rod; R_2 is the inner radius of DMA housing ($R_2/R_1 = 2$); $L = 400$ mm is the distance between the mid-planes of DMA exit slit and inlet slit; $Q_s = 5$ Lpm is the sheath air flow rate.

The extracted particles flow rate (equal to aerosol inlet flow rate) is $Q_o = 0.3$ Lpm. The mobility band relative half-width Q_o/Q_s is selected of 0.06 (0.1 normal) to increase the multiply-charged particles charge determination accuracy.

The particle's electrical mobility is related to a particle charge ez and diameter d via the Stokes law as

$$Z = \frac{ezC_C}{3\pi\mu d}, \tag{2}$$

where z is the number of elementary charges; e is the elementary charge; μ is the gas viscosity; C_C is the Cunningham slip correction factor (Allen & Raabe, 1985):

$$C_C = 1 + 2\frac{\lambda}{d}\left(1.142 + 0.558 \exp\frac{-0.999d}{2\lambda}\right),$$

where the mean free path $\lambda = 67.3$ nm.

The outlet DMA flow (0.3 Lpm) is mixed with the clean air (0.7 Lpm) and this mixture, which contains particles with electrical mobility Z_0, is fed into the laser aerosol spectrometer LAS-P (LAS-P, 2010). This spectrometer (model 9814.290.00) is manufactured by Karpov Institute of Physical Chemistry (Moscow). The multichannel size distribution has the following optical latex-equivalent diameter ranges (μm): 0.15–0.2; 0.2–0.25; 0.25–0.3; 0.3–0.4; 0.4–0.5; 0.5–0.7; 0.7–1.0; 1.0–1.5; >1.5. This spectrometer allows determining the particle size distribution when their number density in a sample flow (1 Lpm) is less than 2×10^3 cm^{-3}. The maximum relative error in determining the particle sizes and their number density is $\pm 5\%$ and $\pm 10\%$, respectively. The different samples were identical in their characteristics during the measuring time, due to the stable operating conditions of a welding fume source.

4. Experimental results and procedure of their processing

The welding fume is obtained when the electrodes Paton UONI 13/55 were used. Such a fume has three-modal particle size distribution (Ennan et al., 2013), where the first two modes are primary particle agglomerates and the third mode is the coarse fume particles (Vishnyakov et al., 2014). Each of these modes is described by the probability density function of log-normal size distribution,

$$f_d = \frac{1}{d\sqrt{2\pi}\ln\sigma_d} \exp\frac{-(\ln d - \ln d_m)^2}{2\ln^2\sigma_d}, \tag{3}$$

where σ_d is the standard deviation; $d_m = \overline{d}\exp(-\ln^2\sigma_d/2)$ is the median of the size distribution; $\overline{d}$ is the average diameter of particles.

The initial particle size distribution (without charging and separation in the DMA) is described by a functions sum (3) with mode fractions:

$$f_d^{Total} = N_1^{In} f_{d1} + N_2^{In} f_{d2} + N_3^{In} f_{d3}, \quad N_1^{In} + N_2^{In} + N_3^{In} = 1. \tag{4}$$

The measurement procedure for obtaining the particle size distribution is described in a paper by Ennan et al. (2013). The modes' parameters for welding fume under consideration are presented in Table 1. The particle size distribution for these parameters is presented in Fig. 3. Charging the particles in the corona ionizer does not influence this distribution. The size distribution of the charged particles, which is obtained by summing the number of particles in each LAS-P channel in the whole range of the DMA voltage and by the normalization of the sums by the total number of particles passing through the ionizer, coincides with the initial distribution. Hence, the particle loss in the ionizer and the DMA does not change the particle size distribution of the welding fume.

Table 1
Parameters of the tree-modal particle size distribution.

Mode number i	Average size $\overline{d}_i$ (nm)	Standard deviation σ_i	Mode fraction N_i^{In}
1	225	1.2	0.755
2	335	1.25	0.242
3	1000	2	0.003

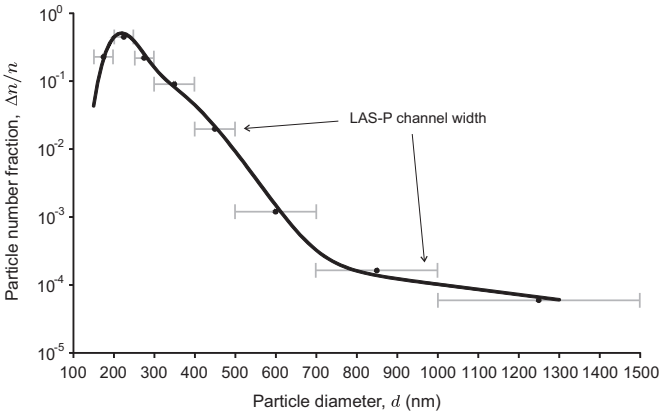

Fig. 3. Initial particle size distribution: dots are experimental data; line is the approximation by Eq. (4).

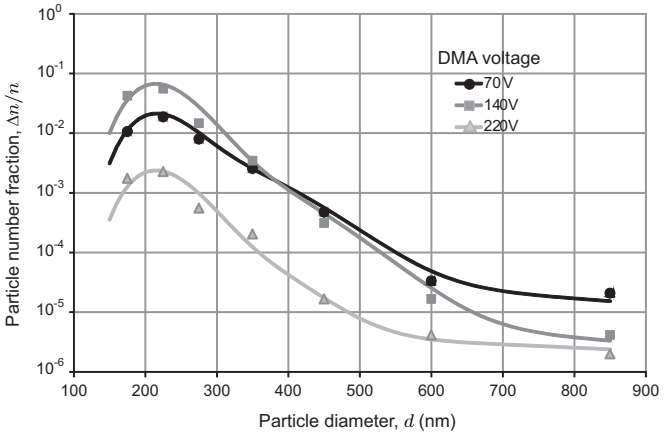

Fig. 4. Examples of particle size distributions for three DMA voltages for the negative corona: dots are experimental data; lines are the approximations by Eqs. (4) and (5) with mode fractions $N_i(U_j)$.

The particles with electrical mobility, which corresponds to the applied voltage (see Eq. (1)), are contained in the outlet DMA flow for each voltage value. The particles with different sizes can have equal mobility, because they can carry different charges. The size distribution of these particles also is described by the function (4), but with its own mode fractions for each DMA voltage $N_i(U_j)$.

This method is illustrated by Figs. 4 and 5. Examples of particle size distributions for three DMA voltages are presented in Fig. 4 for the negative corona. Approximation of experimental data in Fig. 4 is obtained by fitting the values of mode fractions in three-modal distribution (4) under conditions

$$\sum_j N_1(U_j) = N_1^{In}; \quad \sum_j N_2(U_j) = N_2^{In}; \quad \sum_j N_3(U_j) = N_3^{In}; \tag{5}$$

where N_i^{In} are the mode fractions from Table 1; U_j is the voltage applied to DMA; the sums include all the measurement points.

The dependency of the particle charge on its size and DMA voltage can be obtained from Eqs. (1) and (2):

$$z(U,d) = \frac{3\mu Q_s d}{2eC_C LU} \ln\frac{R_2}{R_1}. \tag{6}$$

Therefore, the values of the charge (6) for each DMA voltage can be laid off on the abscissa in Fig. 4 instead of particle sizes. Thus, it is possible to replace the particle size distribution by the particle charge distribution, which is presented in Fig. 5. The increase of DMA voltage leads to decreasing particle fractions with large charge, i.e. with high electrical mobility.

The dependencies of mode fractions on DMA voltage $N_i(U_j)$ can be obtained by approximation of measurements of LAS-P for each mode under conditions (5). The results of these measurements and approximations can be represented as the charge distributions of mode fractions $N_i(U_j)$, because for each mode and for each DMA voltage U_j, the charges (6) are in correspondence with the average particle diameter $\overline{d}_i$.

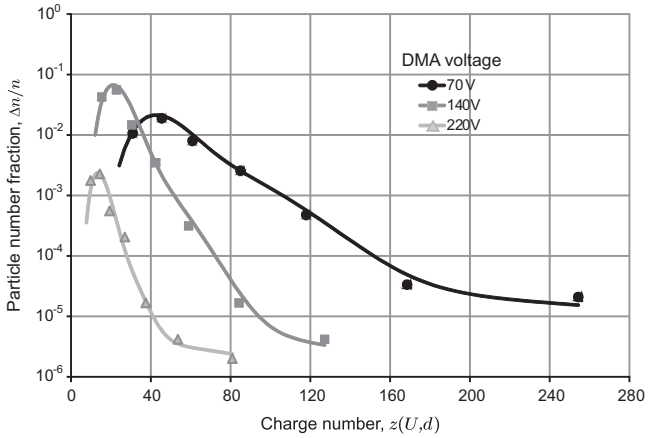

Fig. 5. Particle charge distributions, corresponding to the size distributions in Fig. 4: dots are experimental data; lines are the approximations by Eqs. (4) and (5) with mode fractions $N_i(U_j)$.

Table 2
Mode charges for negative corona and two DMA voltages.

$U = 70$ V			$U = 140$ V		
Mode number i	Average size $\overline{d}_i$ (nm)	Mode fraction N_i	Charge number z_i	Mode fraction N_i	Charge number z_i
1	225	3.8×10^{-2}	46	1.1×10^{-1}	23
2	335	7.5×10^{-3}	80	6.4×10^{-2}	40
3	1000	4.5×10^{-4}	306	1.2×10^{-3}	153

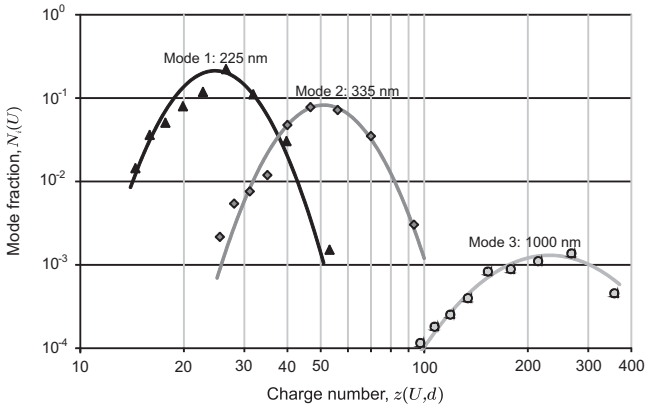

Fig. 6. Dependencies of mode fractions on particle charges for the positive corona: dots are experimental data; lines are the approximations by Eq. (20).

For example, in Table 2 the mode fractions and mode charge numbers are presented, which describe the black curve (DMA voltage is 70 V) and the grey curve (DMA voltage is 140 V) in Figs. 4 and 5.

4.1. Positive corona

The results for the welding fume particles' charging in unipolar charger using a positive corona discharge with a current 0.2 mA are presented below. For positive polarity $(H_3O)^+(H_2O)_n$ and $NH_4^+(H_2O)_n$ are suggested to be most abundant ion species produced in air (Nagato, Tanner, Friedli, & Eisele, 1999; Parts & Luts, 2004; Shanin, 1966).

The particle fraction dependencies on the DMA voltage separately for each mode $N_i(U_j)$ allow us to recover the particle charge distribution for each mode, if instead of U_j one uses the charge expression from Eq. (6) as a function of DMA voltage and of average mode size from Table 1, i.e. $N_i(z_{j,i})$, where $z_{j,i} = z(U_j, \overline{d}_i)$. In this manner, the particle charge distributions for each mode are obtained and presented in Fig. 6.

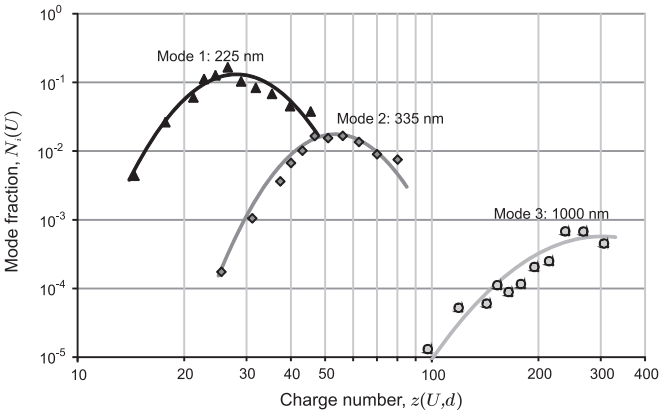

Fig. 7. Dependencies of the mode fractions on the particle charges for the negative corona: dots are experimental data; lines are the approximations by Eq. (20).

4.2. Negative corona

An analogous procedure as is described in Section 4.1 was performed using a negative corona discharge with the same current 0.2 mA, and the results are presented below. Varieties of negative ion species produced by corona sources have been identified. The relative abundance of detected ions varies depending on condition of air used in measurements. Among the detected ions CO_3^-, NO_3^-, HCO_3^- HNO_3 and NO_3^- HNO_3, as well as hydrates of the form $CO_3^-(H_2O)_n$, $NO_2^-(H_2O)_n$, $NO_3^-(H_2O)_n$, NO_3^- $HNO_3(H_2O)_n$ and HCO_3^- $HNO_3(H_2O)_n$ were abundant ion species (Cabane & Playe, 1980; Nagato, Matsui, Miyata, & Yamauchi, 2006; Skanly, Mikoviny, Matejcik, & Mason, 2004, 2008).

After application of the experimental data processing above described procedure, the particle charge distributions for each mode presented in Fig. 7 are obtained.

5. Theory of particle unipolar charging in the dust-ion plasma model

As it follows from experimental data, the particle charges can reach up to several hundreds of elementary charges in a considered system. The Fuchs theory (Fuchs, 1963) is inapplicable in this case, because this theory describes the charging of spherical particles only up to several elementary charges, i.e. is applicable for systems with low ion number density (Biskos et al., 2005a). Therefore, a consideration of the particle charging in approximation of the dust-ion plasma is presented below.

In the corona discharge ionizer of Fig. 1, the voltage is applied between needles of the inner cylinder and the outer cylinder housing. The basic voltage drop takes place near the needle tips, where air ionization by corona discharge occurs. The number density of the single charged ions is about of 10^9–10^{10} cm^{-3} and the number density of the dust particles is about of 10^4–10^5 cm^{-3}, therefore, such a system must be considered as a two-component dust-ion plasma. At the established current the ion number density remains constant in each point of the charging region, except the space charge layer around the particles. Such a system is described by the Poisson equation in the form (Vishnyakov & Dragan, 2006)

$$\nabla^2\varphi = 4\pi e n_{i0}\left(\exp\frac{e\varphi}{k_BT} - 1\right) \text{ for negative ions,} \tag{7a}$$

$$\nabla^2\varphi = 4\pi e n_{i0}\left(1 - \exp\frac{-e\varphi}{k_BT}\right) \text{ for positive ions,} \tag{7b}$$

where φ is the electrical potential; T is the Kelvin temperature; k_B is the Boltzmann constant; n_{i0} is the unperturbed ion number density. In further consideration the singly charged positive ions ($+1$ elementary charge) are assumed for simplicity, i.e. Eq. (7b) will be used.

In general case, the spatial field distribution in the plasma can be described in terms of Jacobi elliptic functions (Vishnyakov & Dragan, 2005). These functions strongly change only near the boundary of the interval under consideration and remain almost constant outside the boundary layer, which is determined by the screening (Debye) length $\lambda_D = \sqrt{k_BT/4\pi e^2 n_{i0}}$ (Fortov, Khrapak, Khrapak, Molotkov, & Petrov, 2004). Therefore, the ion number density can be considered as a constant equal to the unperturbed number density n_{i0} in the charging region.

The average ion number density is equal to their number in the Wigner–Seitz cell (which is a sphere around a particle with radius $R_W = (3/4\pi n_p)^{1/3}$) multiplied by the particle number density n_p:

$$\overline{n}_i = n_p \int_{r_p}^{R_W} n_i(r) 4\pi r^2\, dr = 4\pi n_p n_{i0} \int_{r_p}^{R_W} \exp\frac{-e\varphi(r)}{k_B T} r^2\, dr, \tag{8}$$

where r_p is the particle radius.

Under condition $R_W \gg r_p$, Eq. (7b) yields,

$$\int_{r_p}^{R_W} \exp\frac{-e\varphi(r)}{k_B T} r^2\, dr = \int_{r_p}^{R_W} \left(1 - \frac{1}{4\pi e n_{i0}} \nabla^2 \varphi\right) r^2\, dr = \frac{R_W^3}{3} - \frac{1}{4\pi e n_{i0}} \left(r^2 \frac{d\varphi}{dr}\right)_{r_p}^{R_W} = \frac{1}{4\pi n_p} - \frac{r_p^2 E_p}{4\pi e n_{i0}}, \tag{9}$$

where taken into account that the field at the boundary of a Wigner–Seitz cell $E(R_W) = 0$. The Coulomb field created by the particle is determined by its charge,

$$E_p = \frac{ez}{r_p^2}. \tag{10}$$

Then, from Eqs. (8) to (10) it follows that

$$\overline{n}_i = n_{i0} - z n_p. \tag{11}$$

The particle charge number z is determined by the number of adsorbed ions. The average ion number density remains constant if the ion generation rate is higher than their adsorption rate, i.e. if the particle number density is negligible. But the ion adsorption rate is much higher than their generation rate at high particle number density, because the ion current decrease through the ionizer is observed. In this case it is possible to consider the average ion number density change as a result of adsorption as $\overline{n}_i(t) = n_{ib} - z(t) n_p$, where n_{ib} is the initial number density without particles. As it follows from comparison of this equation with Eq. (11), the unperturbed number density is equal to the initial ion number density $n_{i0} = n_{ib}$ and does not change in the process of particles' charging. It is very important, because the initial number density n_{ib} can be measured by the current through the ionizer without particles.

The electric field is not uniform in the cylindrical symmetry, but within the screening length it can be considered as constant. The field causes the directed motion of ions with the drift velocity $v_{Ei} = Z_i E$, where Z_i is the ion mobility; E is the electric field. The adiabatic approach for particles is used, taking into account the difference between particle and ion masses.

The ion, located near the particle, experiences forces from the external uniform field and from the particle radial field (10). The resultant flux of drifting ions to a particle surface with charge number z is determined by the following equation (Reist, 1984):

$$I_E = \pi e z_{mE} Z_i n_{i0} \left(1 - \frac{z}{z_{mE}}\right)^2, \tag{12}$$

where $z_{mE} = E_{max} r_p^2 / e$ is the saturation charge number of the particle, i.e. the charge at which the particle radial field (10) $E_p = E_{max}$ completely prevents the ion drift to the particle.

Besides the flux (12) there is also the ion diffusion flux towards the particle. This flux is caused by ion adsorption on the particle surface, i.e. their disappearance from the gas phase. The system under consideration is the dust-ion plasma, in which the perturbed region (a space charge layer) is determined by the screening length λ_D. Therefore, the gradient of ion number density near the particle can be determined as a ratio of difference between the unperturbed number density (outside the space charge layer) and the number density of adsorbed ions $z n_p$ to the screening length (the density of adsorbed ions is z/V_p, where $V_p = 1/n_p$ is the particle volume):

$$\nabla n_i = \frac{n_{i0} - z n_p}{\lambda_D}.$$

It should be noted that in plasmas the diffusion regime of particle charging is not determined by the Knudsen number, but by the condition between ion mean free path λ_i and screening length λ_D: $\lambda_i \ll \lambda_D$ (Fortov et al., 2004), which remains valid up to the ion number density 10^{14} cm^{-3}.

The Coulomb force defined by the radial field (10) of a charged particle counteracts the ion diffusion. As a result, the diffusion flux density is determined by the following equation:

$$j_D = \alpha D_i \frac{n_{i0} - z n_p}{\lambda_D} - Z_i z n_p E_p, \tag{13}$$

where $D_i = Z_i k_B T / e$ is the ion diffusivity; α is the relative attachment factor. The material of particles may affect the particle adsorption probability. The attachment factor is used to describe the ratio of adsorbable ion number (ions that are adsorbed by the particle surface), to the total number of ions that impinge upon that surface during the same period of time. The differences in attachment factors for different particles make it very difficult to calculate the effect that polydispersity will have on the charge distribution at different sizes. The relative attachment factor used here is the ratio of adsorption probabilities for negative and positive ions. For particle charging in the positive corona by definition $\alpha = 1$. For charging in the negative corona α may be different because of a negative ion species wide range.

The ion diffusion flux to the surface of a particle with radius a is

$$I_D = 4\pi r_p^2 \alpha Z_i \frac{k_B T}{e} \frac{n_{i0} - z n_p}{\lambda_D} - 4\pi e Z_i z^2 n_p. \tag{14}$$

The flux (14) has a maximum at the initial time moment, when $z=0$ and terminates at the particle saturation charge number

$$z_{mD} = z_0 \left(\sqrt{1 + \frac{2n_{i0}}{z_0 n_p}} - 1 \right), \tag{15}$$

where $z_0 = \alpha r_p^2 k_B T / 2e^2 \lambda_D$.

For conditions: $n_{i0} = 10^{10}$ cm^{-3} and $T = 300$ K, the screening length $\lambda_D \cong 11$ μm. Then $z_0 \sim r_p^2 \cdot 0.8$ μm^{-2}. Equation (15) can be simplified when the particle number density $n_p \ll n_{i0}$:

$$z_{mD} \cong \sqrt{2 z_0 \frac{n_{i0}}{n_p}}. \tag{16}$$

For particle number density $n_p = 10^4$ cm^{-3} the saturation charges are equal $z_{mE} = z_{mD}$ when the field is

$$E = \frac{e}{r_p^2} \sqrt{2 z_0 \frac{n_{i0}}{n_p}} \cong \frac{2\ \mathrm{V}}{r_p} = 20 \frac{\mathrm{kV}}{\mathrm{cm}} \text{ for } r_p = 1\ \mu\mathrm{m}.$$

Such a field cannot be realized in the charging region saturated by ions. Usually the field is less than 1 kV/cm in the charging region. Therefore, the condition $z_{mE} \ll z_{mD}$ is valid. In particular, $z_{mE} = 4 \times 10^{-5} z_{mD}$ for the field $E = 1$ kV/m.

The particle charging rate is determined by the sum of fluxes (12) and (14). But the flux (12) exists only during the initial stage of charging and can be neglected, therefore the charging is produced by the flux (14):

$$\frac{dz}{dt} = \frac{-1}{\tau} \left(z^2 + 2 z_0 z - 2 z_0 \frac{n_{i0}}{n_p} \right), \tag{17}$$

where $\tau = (4\pi e Z_i n_p)^{-1}$ is the time constant (effective charging time which is necessary for saturation charge achievement), which for $n_p = 10^4$ cm^{-3} is equal $\tau \sim 35$ s, i.e. the charge cannot be saturated, while the particle moves through the corona charger. It should be noted that the similar time constant in Eq. (12) contains the ion number density instead of the particle number density as here, and is equal $\tau_E \sim 40$ μs, that is much less than the charging time ($t_I = 80$ ms).

The solution to Eq. (17) is the function:

$$z = -z_0 + (z_{mD} + z_0) \cdot \tanh \left[(z_{mD} + z_0) \frac{t}{\tau} + \operatorname{atanh} \left(\frac{z_0}{z_{mD} + z_0} \right) \right]. \tag{18}$$

It should be noted that morphology of particles (their non-sphericity) cannot influence the applicability of the proposed theory, because the particle size is much less than the particle perturbation area, radius of which is determined by the screening length $\lambda_D \sim 10$ μm.

6. Processing of the experimental data

Charge of a particle with diameter d, which was charged in the corona discharge ionizer, is determined by Eq. (18),

$$z(d) = -z_0 + (z_{mD} + z_0) \cdot \tanh \left[(z_{mD} + z_0) \frac{t_I}{\tau} + \operatorname{atanh} \left(\frac{z_0}{z_{mD} + z_0} \right) \right], \tag{19}$$

where $t_I = 0.08$ s is the charging time, z_0 and z_{mD} are functions of particle diameter.

Particle charging in a bipolar ion atmosphere, which is described by Fuchs (1963), leads to the Gaussian particle charge distribution, because it is an equilibrium process: adsorption of positive and negative ions is equiprobable, i.e. the particle charge has a fluctuation nature. Charging of particles in the unipolar atmosphere is a non-equilibrium process, because the probability of ion adsorption is much more than the probability of ion desorption. Therefore, the particle charge distribution can be described by a log-normal function:

$$f_z = \frac{1}{\sqrt{2\pi} z \ln \sigma_z} \exp \frac{-[\ln z - \ln z_m(d)]^2}{2 \ln^2 \sigma_z}, \tag{20}$$

where $z_m(d) = z_p(d) \exp(-\ln^2 \sigma_z / 2)$ is the charge distribution median, $z_p(d)$ is the function (19).

Distribution (20) is used for experimental data approximation in Figs. 6 and 7 with the standard deviations $\sigma_{z1} = 1.25$, $\sigma_{z2} = 1.26$, $\sigma_{z3} = 1.45$ for positive corona and $\sigma_{z1} = 1.3$, $\sigma_{z2} = 1.28$, $\sigma_{z3} = 1.47$ for negative corona. The mode average sizes $\overline{d}_i$ are used in Eq. (20). The above theory describes the experimental data reasonably well.

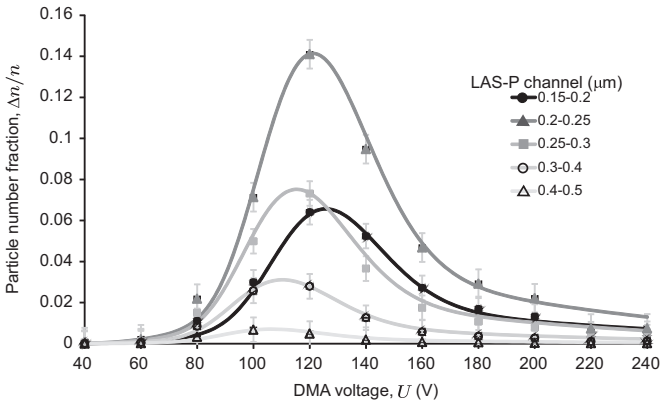

Fig. 8. Dependency of normalized particle number fractions on the DMA voltage for the positive corona: dots are experimental data; lines are the approximations by Eq. (22).

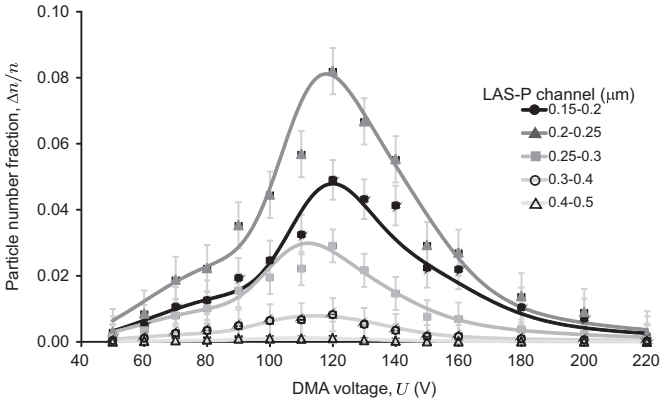

Fig. 9. Dependency of normalized particle number fractions on the DMA voltage for the negative corona: dots are experimental data; lines are the approximations by Eq. (22).

The size distribution and the charge distribution can be combined into a two-dimensional distribution, because for each mode, the density of probability to detect the particle with diameter d and charge number z is determined by the following function, which is the result of multiplication of f_d (3) and f_z (20), with assumption that the distributions are independent:

$$f_{d,z} = \frac{1}{2\pi dz \ln\sigma_d \ln\sigma_z} \exp\frac{-(\ln d - \ln d_m)^2}{2\ln^2\sigma_d} \exp\frac{-[\ln z - \ln z_m(d)]^2}{2\ln^2\sigma_z}, \tag{21}$$

and the resultant distribution function is the sum

$$f(d,z) = C_1 f_{d,z}(\overline{d}_1) + C_2 f_{d,z}(\overline{d}_2) + C_3 f_{d,z}(\overline{d}_3), \tag{22}$$

where the mode fractions for the size and charge distribution obey the relation $C_1 + C_2 + C_3 = 1$.

The linear combination of the three modes (22) fairly describes the measured data which are obtained by using complex DMA+LAS-P. The results of approximations for five channels of LAS-P are presented in Fig. 8 for charging in the positive corona and in Fig. 9 for charging in the negative corona.

It should be noted that attachment factor different values (see Eq. (13)) were used for data approximations which are obtained by using the negative corona (Figs. 7 and 9): $\alpha = 1$ for the first mode; $\alpha = 0.8$ for the second mode; and $\alpha = 1.4$ for the third mode. Such a difference possibly caused by a different chemical compositions of particles of different modes. As it follows from investigations by Vishnyakov, Kiro, & Ennan (2014) and Vishnyakov et al. (2014) for the electrodes Paton UONI 13/55, each mode contains various amounts of elements originating from welding materials, which are determined by their mechanisms of formation. The clusters of the first mode consist mainly of primary particles with size of ~10 nm, which contain ~65% of iron, ~25% of silicon and ~10% manganese. But after air oxidation, these agglomerates contain up to 30% of oxygen (Oprya et al., 2012), thus the resultant iron content in the particles of the first mode is about 45%. The agglomerates of the second mode are associations of first mode cluster and several chain-like agglomerates of nano-sized primary particles with diameter ~2 nm, which contain only 10% of iron and 90% of calcium. As a result, the total iron content in the agglomerates of the second mode is 15–20%. The coarse particles of the third mode contain over 50 % of iron.

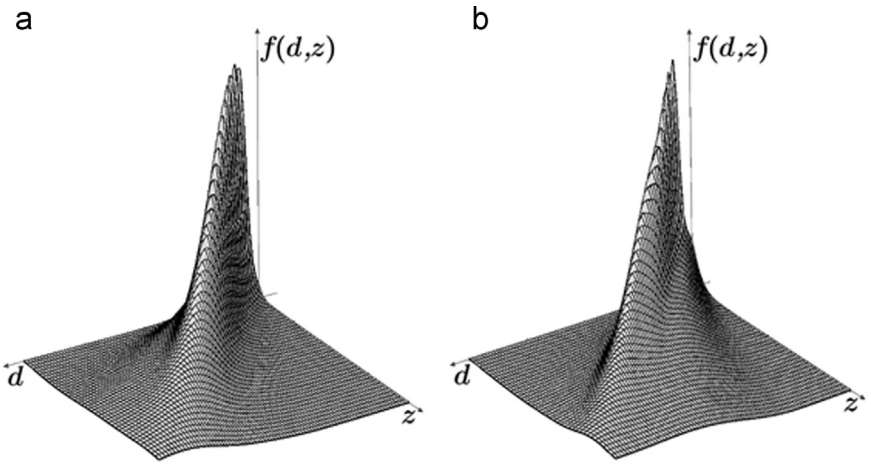

Fig. 10. Size and charge distributions for particles charged in the positive (a) and negative (b) corona.

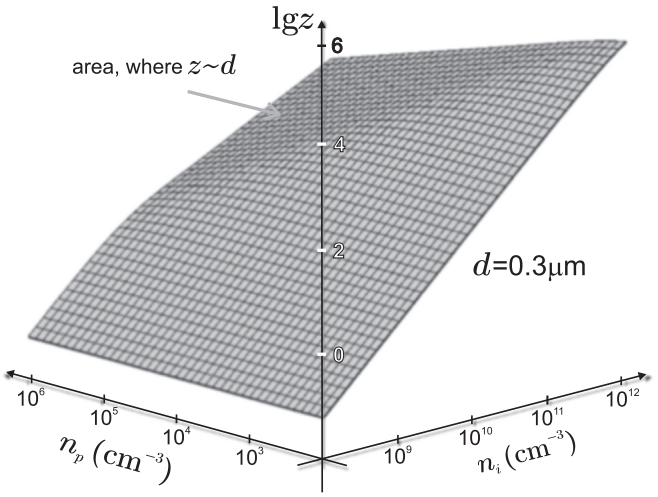

Fig. 11. Dependency of the particle charge on the ion and particle number densities.

Thus, relative attachment factor is correlated with the iron content in the charging particles: possibly the probability of oxygen-containing ions adsorption is proportional to the iron content.

7. Discussion

The presented theory describes well the charging of particles in the corona ionizer with high ion number density, i.e. in the dust–ion plasma. The particle charge distribution is determined by the particle size distribution, because the particle size defines its charge; by the particles' chemical composition, because the latter influences ion adsorption; and by environmental conditions: ion and particle number densities, first of all.

The approximation of experimental data allows constructing the two-dimensional particle size and charge distribution. Such distributions are presented in Fig. 10 for welding fume particles charging in the positive and negative corona. This knowledge should be helpful for the design of electrostatic precipitator.

The dependency of aerosol particle charges on their number density, and dependency of these charges on ion number density in the corona ionizer are also important. These dependencies are presented in Fig. 11 for two particle diameters.

Equation (19) can be simplified for the condition $z_{mD} \gg z_0$,

$$z \cong z_{mD} \cdot \tanh\left(z_{mD}\frac{t_I}{\tau}\right); \tag{23}$$

and for $z_{mD} \ll \tau/t_I \sim 400$, the charge number equals

$$z \sim z_{mD}^2 \frac{t_I}{\tau} = 2z_0 \frac{n_{i0} t_I}{n_p \tau} = \alpha \frac{\pi d^2 D_i n_{i0}}{2\lambda_D} t_I, \tag{24}$$

i.e. the charge of a particle depends only on its surface area and unperturbed (or initial) ion number density and does not depend on the particle number density in the linear approach.

The hyperbolic tangent in (19) tends to 1 under opposite condition $z_{mD} \gg \tau/t_I$, and

$$z \sim z_{mD} = \frac{d}{2e}\sqrt{\frac{\alpha k_B T n_{i0}}{\lambda_D n_p}}, \tag{25}$$

i.e. the charge of a particle linearly depends on its size. In this case there is no dependency on the charging time, because the charge has its maximum value, but the dependency on particle number density appears.

Regime of corona ionizer, which satisfies the latter condition is most preferable for practical applications, as the linear relation between the particle sizes and their charges is optimal for separation of particles by their sizes. This regime is achieved when

$$z_{mD} \frac{t_I}{\tau} = 2\pi d Z_i t_I \sqrt{\frac{\alpha k_B T n_{i0} n_p}{\lambda_D}} \sim 10^{-4} \frac{\mathrm{cm}^{11/4}}{\mathrm{s}} d n_p^{1/2} n_{i0}^{3/4} t_I \gg 1.$$

i.e. increase of both the ion number density and the particle number density leads to realization of such a regime.

For example, when $t_I = 80$ ms and $n_p = 10^4$ cm^{-3}, the ion number density must be $n_i > 3 \times 10^{10}$ cm^{-3} for the particle diameter 1 μm and $n_i > 2.5 \times 10^{11}$ cm^{-3} for the particle diameter 0.2 μm. But, when $n_p = 10^6$ cm^{-3}, the ion number density must be $n_i > 10^9$ cm^{-3} for the particle diameter 1 μm and $n_i > 10^{10}$ cm^{-3} for the particle diameter 0.2 μm.

Thus, the increase of particle number density leads to linearization of the relation between the sizes of particles and their charges. Such relation allows us to separate particles by the sizes in a process of their collection in electrostatic precipitator.

8. Conclusion

The usage of the DMA and LAS-P in tandem allows determining the two dimensional welding fume particle charge and size distribution. The measuring method and procedure of experimental data processing is applicable for any aerosol with particles in the size range 0.15–1.5 μm.

The model of particle charging in the corona discharge in approximation of the dust-ion plasma is in a good agreement with experimental data for welding fume. The proposed measurement technique and the particle charging model allow constructing the two-dimensional size and charge distribution function. It is extremely important for predicting the performance of an electrostatic precipitator for collecting polydisperse particles, not only for welding fumes, but also for any air pollutants.

The chemical composition of the welding fume particles depends on their size (Vishnyakov et al., 2014); and some fractions are valuable for industrial applications. Therefore, the portable electrostatic precipitator with function of the particles' separation by sizes is the most perspective. The increase of the particle number in aerosol and of the ion number in ionizer simplifies the design of such precipitators, because it leads to linearization of the relation between the particle sizes and their charges. Such a relation allows us to separate particles by sizes in the process of their collection, because in this case the dependency of electrical mobility on the particle diameter (2) determines by the Cunningham slip correction factor only, i.e. the electrical mobility $Z(d) \sim 1/d$, and particles with small sizes are collected by grid-type electrostatic filters.

References

Allen, M. D., & Raabe, O. G. (1985). Slip correction measurements of spherical solid aerosol particles in an improved Millikan apparatus. *Aerosol Science and Technology*, *4*, 269–286.

Alonso, M., Santos, J. P., Hontañón, E., & Ramiro, E. (2009). First differential mobility analysis (DMA) measurements of air ions produced by radioactive source and corona. *Aerosol and Air Quality Research*, *9*, 453–457.

Berner, V., & Berner, A. (1982). Mass size distributions and elemental frequency distributions of arc welding smokes. *Journal of Aerosol Science*, *13*, 191–193.

Biskos, G., Reavell, K., & Collings, N. (2005a). Unipolar diffusion charging of aerosol particles in the transition regime. *Journal of Aerosol Science*, *36*, 247–265.

Biskos, G., Reavell, K., & Collings, N. (2005b). Description and theoretical analysis of a Differential Mobility Spectrometer. *Aerosol Science and Technology*, *39*, 527–541.

Cabane, M., & Playe, P. (1980). Mass spectra of negative ions in air-like gas mixtures at atmospheric pressure. *Journal of Aerosol Science*, *11*, 475–482.

Cheng, Y. S., Yeh, H. C., & Kanapilly, G. M. (1981). Collection efficiencies of a point-to-plane electrostatic precipitator. *American Industrial Hygiene Association Journal*, *42*(8), 605–610.

Emets, E. P., Kascheev, V. A., & Poluektov, P. P. (1991). Simultaneous measurement of aerosol particle charge and size distributions. *Journal of Aerosol Science*, *22*, 389–394.

Ennan, A. A., Kiro, S. A., Oprya, M. V., & Vishnyakov, V. I. (2013). Particle size distribution of welding fume and its dependency on conditions of shielded metal arc welding. *Journal of Aerosol Science*, *64*, 103–110.

Fortov, V. E., Khrapak, A. G., Khrapak, S. A., Molotkov, V. I., & Petrov, O. F. (2004). Dusty plasmas. *Physics-Uspekhi*, *47*, 447–492.

Fuchs, N. A. (1963). On the stationary charge distribution on aerosol particles in a bipolar ionic atmosphere. *Pure and Applied Geophysics*, *56*, 185–193.

Hinds, W. C. (1999). *Aerosol technology*. New York: John Wiley& Sons.
Hoppel, W. A., & Frick, G. M. (1986). Ion-aerosol attachment coefficients and the steady-state charge distribution on aerosols in a bipolar ion environment. *Aerosol Science and Technology*, *5*, 1–21.
Knutson, E. O., & Whitby, K. T. (1975). Aerosol classification by electric mobility: Apparatus, theory, and applications. *Journal of Aerosol Science*, *6*, 443–451.
Kruis, F. E., & Fissan, H. (2001). Nanoparticle charging in a twin Hewitt charger. *Journal of Nanoparticle Research*, *3*, 39–50.
Lawless, P. A., & Sparks, L. E. (1988). Modeling particulate charging in ESPs. *IEEE Transactions on Industry Applications*, *24*, 922–925.
LAS-P (2010). *Laser Aerosol Spectrometer (LAS-P) model 9814.290.000*. Moscow: Karpov Institute of Physical Chemistry.
Nagato, K., Tanner, D. J., Friedli, H. R., & Eisele, F. L. (1999). Field measurement of positive ion mobility and mass spectra at a Colorado site in winter. *Journal of Geophysical Research*, *104*, 3471–3482.
Nagato, K., Matsui, Y., Miyata, T., & Yamauchi, T. (2006). An analysis of the evolution of negative ions produced by a corona ionizer in air. *International Journal of Mass Spectrometry*, *248*, 142–147.
Oh, H., Park, H., & Kim, S. (2004). Effects of particle shape on the unipolar diffusion charging of nonspherical particles. *Aerosol Science and Technology*, *38*, 1045–1053.
Oprya, M., Kiro, S., Worobiec, A., Horemans, B., Darchuk, L., Novakovic, V., Ennan, A., & van Grieken, R. (2012). Size distribution and chemical properties of welding fumes of inhalable particles. *Journal of Aerosol Science*, *45*, 50–57.
Parts, T.-E., & Luts, A. (2004). Observed and simulated effects of certain pollutants on small air ion spectra: I. Positive ions. *Atmospheric Environment*, *38*, 1283–1289.
Pohlmann, G., Holzinger, C., & Spiegel-Ciobanu, V. E. (2013). Comparative investigations in order to characterize ultrafine particles in fumes in the case of welding and allied processes. *Welding and Cutting*, *12*(2), 2–10.
Rakitskaya, T. L., Ennan, A. A., Truba, A. S., Kiro, S. A., & Volkova, V. Y. (2014). Physicochemical and catalytic properties of the solid component of welding aerosol. *Chemistry, Physics and Technology of Surface*, *5*(4), 396–403.
Ravent, E. (2006). Controlling chromium fumes. *Welding Journal*, *85*(11), 24–27.
Reist, P. C. (1984). *Introduction to aerosol science*. New York: Macmillan Publishing.
Shanin, M. M. (1966). Mass-spectrometric studies of corona discharges in air at atmospheric pressures. *Journal of Chemical Physics*, *45*, 2600–2605.
Shin, W. G., Wang, J., Mertler, M., Sachweh, B., Fissan, H., & Pui, D. Y. H. (2010). The effect of particle morphology on unipolar diffusion charging of nanoparticle agglomerates in the transition regime. *Journal of Aerosol Science*, *41*, 975–986.
Skanly, J. D., Mikoviny, T., Matejcik, S., & Mason, N. J. (2004). An analysis of mass spectrometric study of negative ions extracted from negative corona discharge in air. *International Journal of Mass Spectrometry*, *233*, 317–324.
Skanly, J. D., Orszagh, J., Mason, N. J., Rees, J. A., Aranda-Gonzalvo, Y., & Whitmore, T. D. (2008). Mass spectrometric study of negative ions extracted from point to plane negative corona discharge in ambient air at atmospheric pressure. *International Journal of Mass Spectrometry*, *272*, 12–21.
Sowards, J. W., Lippold, J. C., Dickinson, D. W., & Ramirez, A. J. (2008a). Characterization procedure for the analysis of arc welding fume. *Welding Journal*, *87* (3), 76–83.
Sowards, J. W., Lippold, J. C., Dickinson, D. W., & Ramirez, A. J. (2008b). Characterization of welding fume from SMAW electrodes—Part I. *Welding Journal*, *87* (4), 106–112.
Sowards, J. W., Ramirez, A. J., Dickinson, D. W., & Lippold, J. C. (2010). Characterization of welding fume from SMAW electrodes—Part II. *Welding Journal*, *89* (4), 82–90.
Tammet, H., Mirme, A., & Tamm, E. (2002). Electrical aerosol spectrometer of Tartu University. *Atmospheric Research*, *62*, 315–324.
Vishnyakov, V. I., & Dragan, G. S. (2005). Electrostatic interaction of charged planes in the thermal collision plasma: Detailed investigation and comparison with experiment. *Physical Review E*, *71*, 016411.
Vishnyakov, V. I., & Dragan, G. S. (2006). Thermoemission (dust-electron) plasmas: Theory of neutralizing charges. *Physical Review E*, *74*, 036404.
Vishnyakov, V. I., Kiro, S. A., & Ennan, A. A. (2014). Multicomponent condensation in the plasma of welding fumes. *Journal of Aerosol Science*, *74*, 1–10.
Vishnyakov, V. I., Kiro, S. A., Oprya, M. V., & Ennan, A. A. (2014). Coagulation of charged particles in self-organizing thermal plasmas of welding fumes. *Journal of Aerosol Science*, *76*, 138–147.